Three-Dimensional Structures Self-Assembled from DNA Bricks

Yonggang Ke *et al.*

Science **338**, 1177 (2012);
DOI: 10.1126/science.1227268

Science (print ISSN 0036-8075; online ISSN 1095-9203) is published weekly, except the last week in December, by the American Association for the Advancement of Science, 1200 New York Avenue NW, Washington, DC 20005.

Three-Dimensional Structures Self-Assembled from DNA Bricks

Yonggang Ke,[1,2,3] Luvena L. Ong,[1,4] William M. Shih,[1,2,3] Peng Yin[1,5]*

We describe a simple and robust method to construct complex three-dimensional (3D) structures by using short synthetic DNA strands that we call "DNA bricks." In one-step annealing reactions, bricks with hundreds of distinct sequences self-assemble into prescribed 3D shapes. Each 32-nucleotide brick is a modular component; it binds to four local neighbors and can be removed or added independently. Each 8–base pair interaction between bricks defines a voxel with dimensions of 2.5 by 2.5 by 2.7 nanometers, and a master brick collection defines a "molecular canvas" with dimensions of 10 by 10 by 10 voxels. By selecting subsets of bricks from this canvas, we constructed a panel of 102 distinct shapes exhibiting sophisticated surface features, as well as intricate interior cavities and tunnels.

Self-assembly of nucleic acids (DNA and RNA) provides a powerful approach for constructing sophisticated synthetic molecular structures and devices (*1*–*31*). Structures have been designed by encoding sequence complementarity in DNA strands in such a manner that by pairing up complementary segments, the strands self-organize into a prescribed target structure under appropriate physical conditions (*1*). From this basic principle, researchers have created diverse synthetic nucleic acid structures (*27*–*30*) such as lattices (*4*, *6*, *8*–*10*, *25*), ribbons (*15*), tubes (*6*, *15*, *25*, *26*), finite two-dimensional (2D) and 3D objects with defined shapes (*2*, *9*–*11*, *13*, *16*–*19*, *22*, *23*, *26*), and macroscopic crystals (*20*). In addition to static structures, various dynamic systems have been constructed (*31*), including switches (*5*), walkers (*7*, *14*, *21*), circuits (*12*, *14*, *24*), and triggered assembly systems (*14*). Additionally, because DNA and RNA can be interfaced with other functional molecules in a technologically relevant fashion, synthetic nucleic acid structures promise diverse applications; researchers are using nucleic acid structures and devices to direct spatial arrangement of functional molecules (*6*, *25*, *32*–*34*), facilitate protein structure determination (*35*), develop bioimaging probes (*33*, *34*), study single-molecule biophysics (*36*), and modulate biosynthetic and cell-signaling pathways (*25*, *37*).

An effective method for assembling megadalton nanoscale 2D (*11*) and 3D shapes (*16*–*19*, *23*) is DNA origami (*29*), in which a long "scaffold" strand (often a viral genomic DNA) is folded to a predesigned shape via interactions with hundreds of short "staple" strands. However, each distinct shape typically requires a new scaffold routing design and the synthesis of a different set of staple strands. In contrast, construction from standardized small components (such as DNA tiles) that each can be included, excluded, or replaced without altering the rest of the structure—modular assembly—offers a simpler approach to constructing shapes. In addition, if all components are short strands that can be chemically synthesized, the resulting structures would have greater chemical diversity than DNA origami, which typically contains half biological material (the scaffold) in mass and half synthetic material (the staples). A variety of structures have been assembled by using DNA (*3*, *4*, *6*, *8*, *10*, *13*, *15*, *20*) and RNA (*9*, *22*, *25*) tiles, including periodic (*4*, *6*, *25*) and algorithmic (*8*) 2D lattices, extended ribbons (*15*) and tubes (*6*, *15*, *25*), 3D crystals (*20*), polyhedra (*13*, *22*), and finite 2D shapes (*9*, *10*). However, modular self-assembly of finite-sized, discrete DNA structures has generally lacked the complexity that DNA origami can offer.

Only recently have researchers demonstrated finite complex 2D shapes (*26*) self-assembled from hundreds of distinct single-stranded tiles (SSTs) (*15*). Unlike a traditional multistranded tile (*3*, *4*, *6*, *8*–*10*, *13*, *20*, *25*), which is a well-folded, compact structure displaying several sticky ends, an SST is a floppy single-strand DNA composed entirely of concatenated sticky ends. In one-pot reactions, hundreds of SSTs self-assemble into desired target structures mediated by inter-tile binding interactions; no scaffold strand is required. The simplicity and modularity of this approach allowed the authors to build more than 100 distinct shapes by selecting subsets of tiles from a common 2D "molecular canvas." This latest success has challenged previous thinking that modular components, such as DNA tiles, are not suitable for assembling complex, singularly addressable shapes (*38*). This presumption was largely based on a supposed technically challenging requirement for perfect strand stoichiometry (the relative ratio of the strands). Deviations from equality were expected to result in predominating partial structure formation (*38*). The surprising success of SST assembly may have bypassed this challenge via putative slow and sparse nucleation followed by fast growth (*26*), so that a large number of particles complete their formation well before depletion of the component strand pool.

Here, we generalize the concept of single-stranded "tiles" to "bricks" and thus extend our modular-assembly method from 2D to 3D. A canonical DNA brick is a 32-nucleotide (nt) single strand with four 8-nt binding domains (sticky ends). In simple one-step annealing reactions, prescribed target 3D structures self-assemble robustly from hundreds of unpurified brick strands that are mixed together with no tight control of stoichiometry. The modularity of our method enabled the construction of 102 distinct structures by simply selecting subsets of bricks from a common 3D cuboid molecular canvas consisting of 1000 voxels (fig. S1) (*39*); each voxel fits 8 base pairs (bp) and measures approximately 2.5 by 2.5 by 2.7 nm. These structures include solid shapes, with sophisticated geometries and surface patterns and hollow shapes, with intricate tunnels and enclosed cavities. Additionally, we have constructed structures with alternative packing geometries or using noncanonical brick motifs, demonstrating the method's versatility. The work here thus establishes DNA bricks as a simple, robust, modular, and versatile framework for constructing complex 3D nanostructures by using only short synthetic DNA strands. More generally, it demonstrates how complex 3D molecular structures can be assembled from small, modular components mediated strictly by local binding interactions.

Design of DNA-Brick Structures and a 3D Molecular Canvas

In our design, a DNA brick is a 32-nt strand that we conceptualize as four consecutive 8-nt domains (Fig. 1A). Each DNA brick bears a distinct nucleotide sequence. All DNA bricks adopt an identical shape when incorporated into the target structure: two 16-nt antiparallel helices joined by a single phosphate linkage. The two domains adjacent to the linkage are designated as "head" domains, and the other two are designated as "tail" domains. A DNA brick with a tail domain bearing sequence "a" can interact productively with a neighboring brick with a complementary "a*" head domain in a stereospecific fashion. Each pairing between bricks defines three parallel helices packed to produce a 90° dihedral angle (Fig. 1B, top); this angle derives from the approximate 3/4 right-handed helical twist of 8 bp of DNA.

We introduce a LEGO-like model to depict the design in a simple manner (Fig. 1B, bottom). The model intentionally overlooks the detailed helical

[1]Wyss Institute for Biologically Inspired Engineering, Harvard University, Boston, MA 02115, USA. [2]Department of Cancer Biology, Dana-Farber Cancer Institute, Harvard Medical School, Harvard University, Boston, MA 02115, USA. [3]Department of Biological Chemistry and Molecular Pharmacology, Harvard Medical School, Harvard University, Boston, MA 02115, USA. [4]Harvard–Massachusetts Institute of Technology (MIT) Division of Health Sciences and Technology, MIT, Cambridge, MA 02139, USA. [5]Department of Systems Biology, Harvard Medical School, Harvard University, Boston, MA 02115, USA.

*To whom correspondence should be addressed. E-mail: py@hms.harvard.edu

structure and strand polarity but preserves the aspect ratios and some of the orientational constraints on interactions between DNA bricks: The two protruding round plugs, pointing in the same direction as the helical axes, represent the two tail domains; the two connected cubes with recessed round holes represent the two head domains. A brick must adopt one of two classes of orientation, horizontal or vertical (Fig. 1B). The two bricks connect to form a 90° angle via hybridization, represented as the insertion of a plug into a hole. An insertion is only allowed between a plug and a hole that carry complementary sequences with matching polarity (which is not graphically depicted in the current model for expositional simplicity). In fig. S2, we present a more detailed LEGO-like model that explicitly tracks the polarity of the DNA bricks and their stereospecific interaction pattern.

Structural periodicities of the design are illustrated in a 6H (helix) by 6H (helix) by 48B (bp) cuboid structure (Fig. 1, C and D). Bricks can be grouped into 8-bp layers that contain their head domains. Bricks follow a 90° counterclockwise rotation along successive 8-bp layers, resulting in a repeating unit with consistent brick orientation and arrangement every four layers. For example, the first and fifth 8-bp layers in Fig. 1D share the same arrangement of bricks. Within an 8-bp layer, all bricks share the same orientation and form a staggered arrangement to tile the layer. On the boundary of each layer, some DNA bricks are bisected to half-bricks, representing a single helix with two domains. The cuboid is self-assembled from DNA bricks in a one-step reaction. Each brick carries a particular sequence that directs it to fit only to its predesigned position. Because of its modular architecture, a predesigned DNA brick structure can be used for construction of smaller custom shapes assembled from subsets of DNA bricks (Fig. 1E). Detailed strand diagrams for the DNA brick structures are provided in figs. S3 and S4.

3D molecular canvas. The LEGO-like model can be further abstracted to a 3D model that contains only positional information of each 8-bp duplex. A 10H by 10H by 80B cuboid is conceptualized as a 3D molecular canvas that contains 10 by 10 by 10 voxels. Each voxel fits an 8-bp duplex and measures 2.5 by 2.5 by 2.7 nm (Fig. 1F). Based on the 3D canvas, a computer program first generates a full set of DNA bricks, including full-bricks and half-bricks that can be used to build a prescribed custom shape. Using 3D modeling software, a designer then needs only to define the target shapes by removing unwanted voxels from the 3D canvas—a process resembling 3D sculpting. Subsequently, the computer program analyzes the shape and automatically selects the correct subset of bricks for self-assembly of the shape.

Self-Assembly of DNA-Brick Cuboid Structures

Using the above design strategy, we constructed a wide range of DNA brick structures (*39*). We

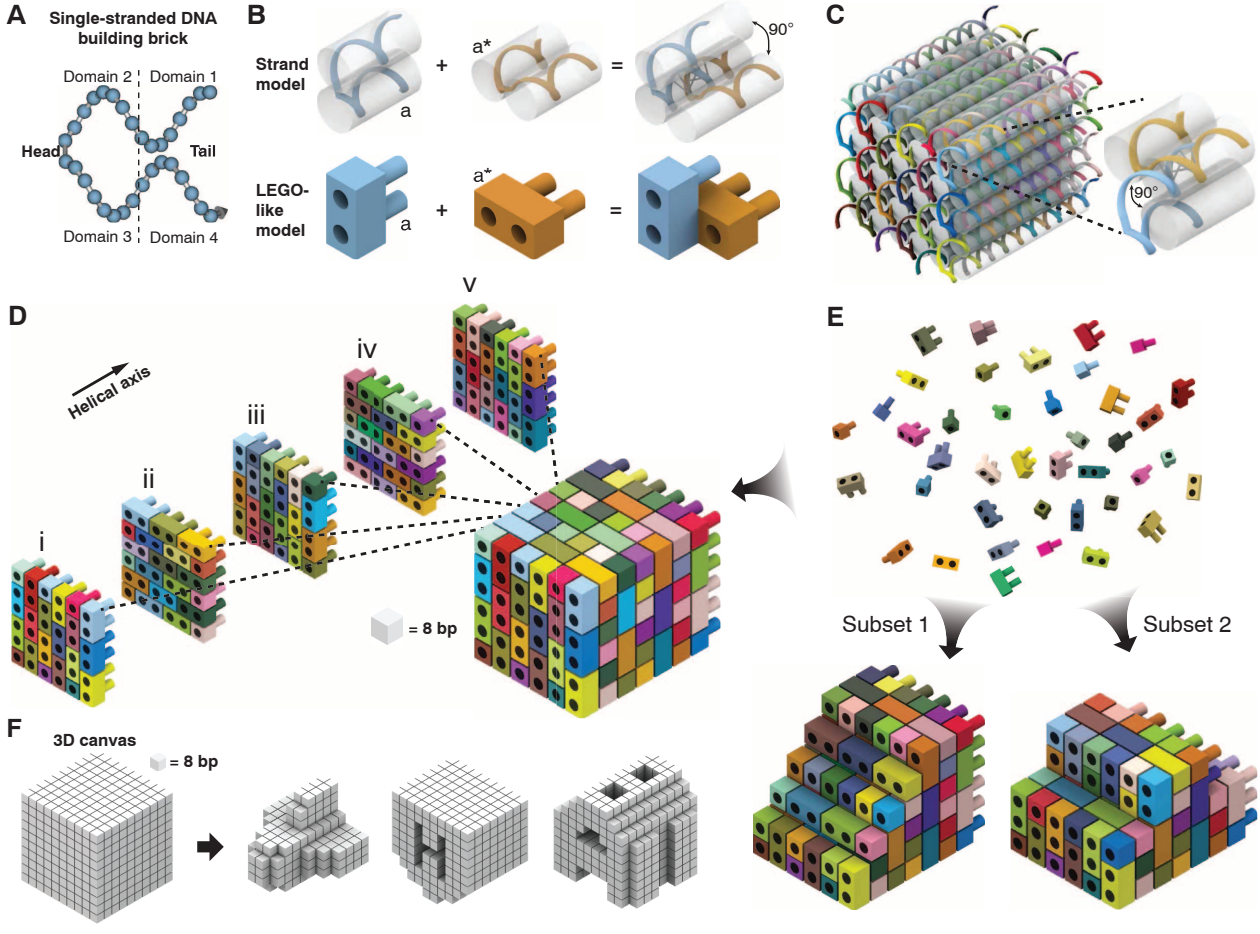

Fig. 1. Design of DNA brick structures analogous to structures built of LEGO® bricks. (**A**) A 32-nt four-domain single-stranded DNA brick. Each domain is 8 nt in length. The connected domains 2 and 3 are "head" domains; domains 1 and 4 are "tail" domains. (**B**) Each two-brick assembly forms a 90° dihedral angle via hybridization of two complementary 8-nt domains "a" and "a*". (**C**) A molecular model that shows the helical structure of a 6H by 6H by 48B cuboid 3D DNA structure. Each strand has a particular sequence, as indicated by a distinct color. The inset shows a pair of bricks. (**D**) A LEGO-like model of the 6H by 6H by 48B cuboid. Each brick has a particular sequence. The color use is consistent with (B). Half bricks are present on the boundary of each layer. (**E**) The 6H by 6H by 48B cuboid is self-assembled from DNA bricks. The bricks are not interchangeable during self-assembly because of the distinct sequence of each brick. Using the 6H by 6H by 48B as a 3D molecular canvas, a smaller shape can be designed by using a subset of the bricks. (**F**) 3D shapes designed from a 10 by 10 by 10–voxel 3D canvas; each voxel fits 8 bp (2.5 nm by 2.5 nm by 2.7 nm).

first constructed 3D cuboid structures of a variety of sizes and aspect ratios (Fig. 2).

Random sequence design. The sequences of DNA bricks were designed by random assignments of base pairs (A-T, C-G) to 3D structures. We first tested two versions of a 6H by 6H by 64B cuboid, with either random sequences or specially designed sequences (designed by smoothing binding energy, minimizing undesired secondary structure, and reducing sequence symmetry) and observed comparable self-assembly yields (fig. S5). We also tested three sets of random sequences using a 4H by 12H by 120B cuboid and again observed similar assembly yields (figs. S6 and S7; more discussion on domain similarity of random sequence design is provided in fig. S8). Thus, random sequences were applied to all subsequent designs.

Protector bricks. Including unpaired single strands at the ends of DNA duplexes has proven to be effective for mitigating unwanted aggregation that results from blunt-end stacking (*11*). An 8-nt single-stranded domain protruded out from every 5′ or 3′ end of all DNA duplexes in our 3D structure designs (Fig. 1C). The sequences of these 8-nt domains were replaced with eight continuous thymidines to further prevent undesired nonspecific binding interactions between exposed single-stranded domains. DNA bricks with modified head or tail poly-T domains are named "head protectors" or "tail protectors," respectively.

Boundary bricks. A 16-nt half brick could be merged with a preceding 32-nt full brick along the direction of its helix to form a 48-nt strand (figs. S9 to S11). We observed a 1.4-fold improvement in assembly yield for a 6H by 6H by 64B cuboid when this 48-nt boundary-strand design was implemented, possibly reflecting accelerated nucleation of target structure formation. Hence, this merge strategy was applied to all of our 3D structures.

Assembly and characterization of 6H by 10H by 128B cuboid. For a detailed characterization study, we constructed a 6H by 10H by 128B cuboid (Fig. 2A). It consists of 459 strands (7680 bp, with a molecular weight comparable with that of an M13-based DNA origami; design details are provided in figs. S12 and S13). Unpurified DNA strands were mixed together at nominally equal ratios without careful adjustment of stoichiometry (*39*). To determine the optimal assembly conditions, we tested two annealing ramps (24-hour annealing and 72-hour annealing), two strand concentrations (100 and 200 nM per strand), and eight $MgCl_2$ concentrations (10, 20, 30, 40, 50, 60, 70, and 80 mM). Equal amounts of each sample (2 pmol per strand) were then subjected to EtBr-stained 2% agarose gel electrophoresis (fig. S14). The best gel yield (~4% as calculated by yield = measured mass of product/mass of all strands) was achieved at the following conditions: 200 nM per strand, 72-hour annealing, 40 mM $MgCl_2$ (fig. S15). The above gel yield reflects only an approximate estimate for the incorporation ratio of the monomer strands (*26*).

For comparison, 4 to 14% gel yield was reported for 3D DNA origami with similar size and aspect ratios [such as the 10H by 6H by 98B and other origami cuboids in (*40*)]. The origami gel yield was estimated as yield = (scaffold strands incorporated into product/total scaffold strands); the loss of excessive staple strands (normally 5- to 10-fold more than the scaffold strand) was not taken into account. For DNA bricks, the optimal 40 mM $MgCl_2$ was higher than the optimal $MgCl_2$ concentration for 3D origami folding, which typically is below 30 mM (*18*). Column-purified DNA bricks product (~50% recovery efficiency) (Fig. 2B) migrated as a single band on agarose gel and appeared under transmission electron microscopy (TEM) with expected morphology (Fig. 2C) and measured dimensions of 0.34 nm (± 0.01 nm SD) per base pair and 2.5 nm (± 0.2 nm SD) per helix width. For the gel-purified product, "the percentage of intact structures" was estimated at 55% by counting the ratio of intact particles over all the particles in TEM images (fig. S16). This percentage of intact structures is comparable with the previously reported percentages of 3D square-lattice DNA origami (27% for a 6H by 12H by 80B cuboid, 59% for an 8H by 8H by 96B cuboid) (*41*).

Special designs can be applied to increase the assembly yield of the 6H by 10H by 128B cuboid. "Head protectors" and "tail protectors" appeared especially unstable because half of their 8-nt domains are unpaired. By merging "head protectors" of the 6H by 10H by 128B cuboid with their neighboring strands (figs. S17 and S18), a modified version 6H by 10H by 128B-M cuboid was obtained and showed 190% improvement in gel assembly yield and 17% improvement in the percentage of intact structures under TEM over the standard 6H by 10H by 128B cuboid (fig. S19). Thus, 3D structures can be further stabilized by using special design rules, such as this merging strategy. However, this modification requires deletions of crossovers between helices, which may potentially create global or local deformations, and was not used for constructions in the remainder of the paper.

Structures of different sizes. Eighteen distinct cuboid structures that contain 9, 16, 36, 60, 96, and 144 helices were designed, annealed using the optimal conditions previously identified for the 6H by 10H by 128B cuboid self-assembly, and characterized through gel and TEM (Fig. 2D and

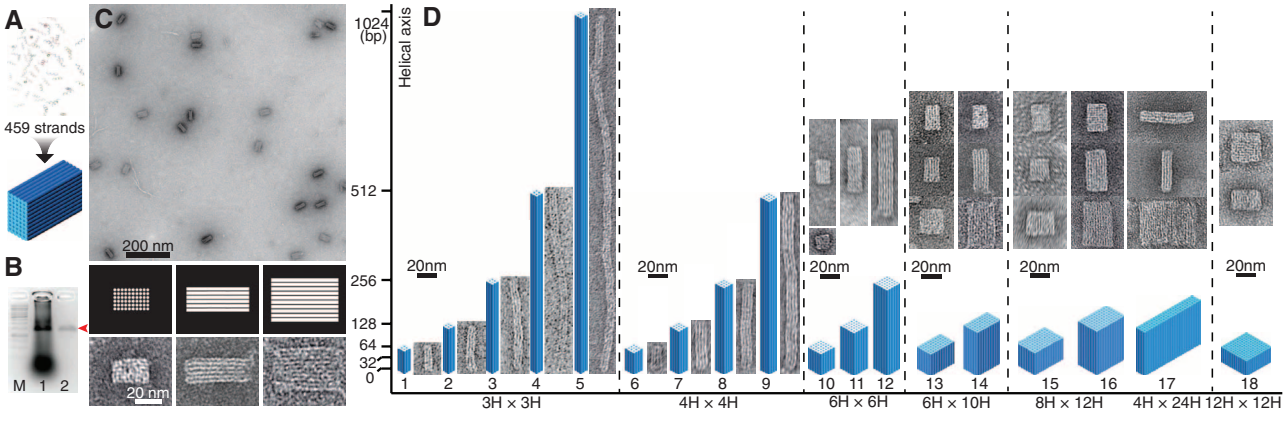

Fig. 2. Cuboid structures self-assembled from DNA bricks. (**A**) DNA bricks self-assembled into a 6H by 10H by 128B cuboid in a one-step thermal annealing process. (**B**) Agarose gel electrophoresis showing 50% purification recovery efficiency of the 6H by 10H by 128B cuboid. Lane M contains the 1-kb ladder. Lanes 1 and 2 contain unpurified and purified 6H by 10H by 128B cuboid structures, respectively. The red arrow points to the cuboid product band. (**C**) TEM images of gel-purified 6H by 10H by 128B cuboid. Zoomed-in images (bottom) and corresponding computer-generated graphics (middle) show three different projection views. (**D**) Designs and TEM images of 18 cuboids of a variety of dimensions. Horizontal axis is labeled with the cross-section dimensions of the cuboids; vertical axis is labeled with the lengths of the constituent helices. The lengths are 48B (shape 18), 64B (shapes 1, 6, 10, 13, and 15), 120B (shapes 16 and 17), 128B (shapes 2, 7, 11, and 14), 256B (shapes 3, 8, and 12), 512B (shapes 4 and 9), and 1024B (shape 5). Each 3D cylinder model is drawn proportionally to the relative dimensions of the cuboid; corresponding TEM images are shown to the right or above each model.

fig. S20). Additional TEM images are shown in figs. S21 to S27. Measured dimensions of intact particles for each structure agree with the designs (fig. S28). Gel yields varied from <1 to ~80% (figs. S20C and S28). For structures with the same number of helices, smaller cuboids exhibited higher assembly yields. The highest yield (80%) was observed for the smallest object, the 3H by 3H by 64B cuboid; the lowest yields (<1%) were observed for the 8H by 12H by 120B, 4H by 24H by 120B, and 12H by 12H by 48B cuboids. The biggest DNA objects constructed in this paper are an 8H by 12H by 120B cuboid (formed by 728 strands) and a 4H by 24H by 120B cuboid (formed by 710 strands), which are identical in molecular weight (24,576 nt, 8 MD, and 60% more massive than an M13-based DNA origami). Increasing the concentration for the brick strands helped to increase the yield for a small cuboid, 4H by 4H by 128B (fig. S29). In some cases, higher molecular weight bands can be detected above the product band; these bands are likely multimers caused by nonspecific interactions between assembled products. For example, for the 6H by 10H by 64B structure, TEM revealed that an upper band contained dimers of the cuboids (fig. S30). Cuboids with 32-bp (32B) helices were also tested but failed to assemble (fig. S20). This is likely due to the fact that these cuboids contained only one crossover between each pair of neighboring helices and hence were less stable.

Complex Shapes Made from a 10 by 10 by 10–Voxel 3D Canvas

Using the 10 by 10 by 10–voxel 3D canvas (Figs. 1F and 3A and fig. S31), we next constructed 102 distinct shapes (Fig. 3), demonstrating the modularity of the DNA brick strategy.

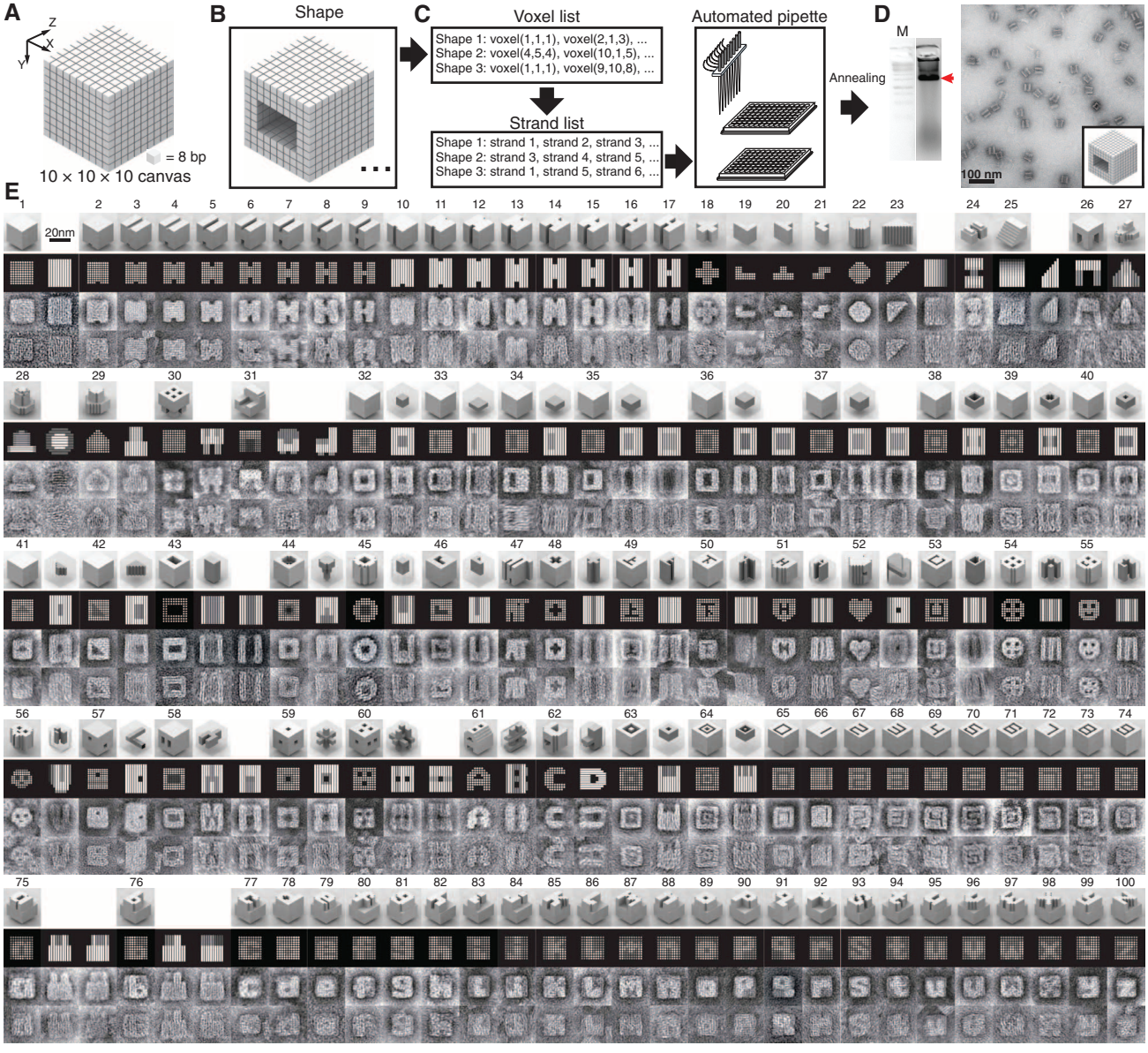

Fig. 3. Shapes made from a 3D molecular canvas. (**A**) A 10 by 10 by 10–voxel 3D canvas. *z* axis is the helical axis. Each voxel (8 bp) measures 2.5 by 2.5 by 2.7 nm. (**B**) Shapes are designed by editing voxels by using 3D modeling software. (**C**) A computer program recognizes the voxel composition of each shape and generates a list of strands to form this shape. The list then is used to direct an automated liquid-handling robot to mix the strands. (**D**) After annealing, the shapes are characterized by means of agarose gel electrophoresis and TEM imaging. Lane M contains the 1-kb ladder. The product band is indicated by the red arrow. (**E**) Computer-generated models and TEM images of shapes. The top row for each shape depicts a 3D model, followed by a computer-generated projection view, an image averaged from six different particles visualized by using TEM, and a representative raw TEM image. More raw images are shown in figs. S38 to S54. In a number of cases, multiple projections are presented. Some shapes with cavities or tunnels are depicted with additional transparent 3D views that highlight the deleted voxels (colored dark gray). For example, the top right model of shape 32 shows the enclosed cuboid cavity.

DNA bricks and derivatives. Any brick in the 3D canvas can become either a boundary half brick (exposed at the edges of a layer and bisected) (Fig. 1D), a protector brick (located in the first or last layer along *z* axis), or even both at same time, in a custom shape design. Thus, modified versions of each brick were generated with all combinations of domain-deletion (bisect to a half-brick), polythymidine-sequence-substitution (change to protector bricks), and boundary-brick-merger (change to 48-nt boundary bricks) to accommodate the possibilities (two types of strands with low occurring frequency and four types of strands with only one binding domain were excluded in our implementation) (fig. S32). Overall, a master collection of 4455 strands (with a total of 138,240 nt) were generated by a computer program to guarantee that a designed shape could be assembled with head/tail protector bricks and 48-nt boundary bricks. Custom shapes were assembled via selecting subsets of the master collection without synthesizing new strands.

Automated design process. By rendering the 3D canvas using 3D modeling software, we can edit voxels and visualize a shape using a graphical user interface (Fig. 3B). Then, the voxel information of multiple shapes is interpreted by a custom program to generate a list of strands involved in the formation of each shape. This list is subsequently processed to direct an automated liquid-handling robot to select DNA strands from source plates and pipette them to the wells of a product plate, mixing strands for many shapes in a high-throughput manner (Fig. 3C). The strands will be subsequently annealed in separate test tubes to produce the desired structures (Fig. 3D). The complete design workflow is shown in figs. S33 and S34. To use existing computational tools previously developed by other researchers, we can also convert shapes to caDNAno files (*40*). Each shape's conformation then can be simulated using CanDo (*42*), a software tool for computing 3D structures of DNA origami (fig. S35).

Using the 3D canvas and following the automated design process, we successfully constructed 102 distinct shapes (gels in figs. S36 and S37; TEM images of shapes 1 to 100 in Fig. 3E; and raw TEM images for all the shapes in figs. S38 to S54).

Shapes 1 to 17. The basic design constraints were studied by using a group of shapes containing two 4H by 10H by 80B blocks connected by a middle "connecting block" (shapes 2 to 17). The connecting blocks were two-voxel wide along *x* axis and systematically designed to possess decreasing numbers of voxels along *y* axis (shapes 2 to 9) or *z* axis (shapes 10 to 17). Eliminating voxels along the *x* axis should have the same effect as eliminating voxels along the *y* axis because of the shape symmetry. Agarose gel electrophoresis revealed that in both systems, as the connector became overly thin, the gel yields for the intact structures decreased, and partial structures (putative unconnected 4H by 10H by 80B blocks) became more prominent (for example, in lanes for shapes 8, 9, and 15 to 17 in fig. S36). However, reducing the number of voxels along the *z* axis appeared to decrease the yield more significantly than along the *y* axis. Shape 9, which contained only a 2-voxel connection along the *y* axis, gave 6% gel yield. In contrast, the yield for shape 17 (2-voxel along the *z* axis) dropped to 1%. Overall, these observations suggest safe design criteria of at least two continuous voxels along the *x* axis or *y* axis (2 helices) and three *z* axis voxels (24 bp) for stable features. However, as demonstrated in following experiments, smaller features (for example, two *z* axis voxels, shapes 33 to 37; one *x* axis or *y* axis voxel, shapes 64 to 74) can still stably exist in certain shapes in which these features are presumably reinforced by other voxels in close proximity.

Solid shapes 18 to 31. A number of solid shapes were designed including *z* direction extrusions of simple geometric shapes (shapes 18 to 23) and more intricate objects (shapes 24 to 31; also, shape 102 in fig. S54). Gel yields and TEM images of these objects provided more knowledge of the design space of our methodology. For example, shapes 26 and 27, which both contained 3-helix-thick appendages anchored only on one edge, were occasionally found without these protrusions or with them but containing defects. Thus, such thin features, although obeying our design criteria, appeared to be less stable than were the better-supported or thicker features.

Closed-cavity shapes 32 to 42. Previously, a few examples of 3D DNA origami with closed cavities were demonstrated, including a box (*16*), a tetrahedron (*17*), a sphere, and an ellipsoid (*23*). We created a series of "empty boxes" with different sizes of cuboid cavities (shapes 32 to 37) as well as more intricate cavity shapes (such as a square ring, cross, and triangle; shapes 38 to 42).

Open-cavity shapes 43 to 62. We constructed shapes with a single open cavity (tunnel) of varying width, depth, and geometry (shapes 43 to 53) and multiple-parallel cavities (shapes 54 to 56). Shapes with noncrossing perpendicular tunnels (shape 57), turning and branching tunnels (shape 58), and crossing tunnels (shapes 59, 60; also, shape 101 in fig. S54) were also demonstrated. Furthermore, we constructed tunnel-containing cuboids with modified outer surfaces in order to create varying external views from different angles, as demonstrated by shapes 60 to 62.

Features-on-solid-base shapes 63 to 100. Sophisticated features were designed on a solid base, including a full set of 10 Arabic numerals (shapes 65 to 74) and 26 lowercase letters for the English alphabet (shapes 75 to 100). Two concentric ring structures (shapes 63 and 64) and the numerals (shapes 65 to 74) contained features as thin as one voxel (2.5 nm), suggesting that the design criteria (for example, thin structures tend to fail) are contingent on the surrounding environment of a particular feature. These shapes also highlight the capacity of creating extruded features that would otherwise be unattainable via 2D assembly (*26*).

For most shapes, assembly yields were between a few percent and 30% [figs. S36 and S37; in comparison, yields of five 3D DNA origami structures were reported as 7 to 44% (*18*)]. Only five shapes had assembly yields higher than 30%; three shapes had assembly yields lower than 1%.

In spite of our success in making a variety of intricate 3D shapes, some shapes exhibited undesired properties. For example, shapes 60 to 62 only showed <1% of intact particles in TEM images; some fine features of a shape (such as the two wings of shape 27) could be damaged or even completely missing if the shape was extracted from an agarose gel band. We also observed four failed designs that did not produce clear product bands on agarose gels (fig. S55A). Two features-on-solid-base designs showed strong bands on agarose gels (fig. S55B), and were of the expected size in TEM images. However, their features were not clearly resolved under TEM, suggesting that the shapes may have formed, but the features were too subtle to be visualized.

Generality of DNA Brick Self-Assembly

To explore the generality of the DNA brick assembly framework, we constructed structures with brick motifs other than the 32-nt canonical brick motif. These structures include those with alternative lattice geometries that have been previously demonstrated by DNA origami (*11*, *18*, *43*).

Single-layer (2D) structures. Conceptually, a single-layer structure can be constructed by "extraction" of a layer from a 3D brick structure [Fig. 4A and fig. S56, comparison with a 2D single-stranded tile rectangle design (*26*)]. A 30H by 1H by 126B rectangle was intentionally modified to be 10.5 bp per turn instead of 10.67 bp per turn (for 3D design) in order to get a relatively flat structure (fig. S57). Gel yield was estimated to be 18% (fig. S58), which is comparable with 2D single-stranded tile structures (*26*). TEM (Fig. 4B) and atomic force microscopy (AFM) (Fig. 4C) revealed expected rectangle structures. On the basis of AFM images, the dimensions were measured as 0.31 nm (± 0.01 nm SD) per base pair and 2.6 nm (± 0.3 nm SD) per helix width.

3D honeycomb-lattice structures. We then created 10.8-bp per turn (33.3° twist per base pair) honeycomb-lattice (HC) and hexagonal-lattice (HL) DNA structures. Four types of four-domain DNA strands were designed for HC structures (Fig. 4, D and E). A 6H by 6H by 84B-HC structure was successfully constructed and characterized (Fig. 4F and fig. S59). Particles in TEM images were measured to be 13 nm (± 0.9 nm SD) by 22 nm (± 1.0 nm SD) by 29 nm (± 1.2 nm SD). Assembly yield was estimated to be 30% (fig. S60).

3D hexagonal-lattice DNA structures. Two types of strands are used to build a HL structure: a linear strand with multiple 9-nt domains and an 18-nt strand with two 9-nt domains that are connected by a crossover (Fig. 4, G and H).

A 6H by 7H by 108B-HL structure was constructed and characterized (Fig. 4I and fig. S61). Particles in TEM images were measured to be 13 nm (± 0.8 nm SD) by 18 nm (± 1.1 nm SD) by 35 nm (± 2.2 nm SD). Assembly yield was estimated to be 26% (fig. S62).

Other brick motifs. We also constructed a 6H by 10H by 64B cuboid that arranges brick strands in an alternating fashion between layers (figs. S63 and S64) and two 6H by 6H by 64B cuboids that implement two other brick motif designs (figs. S65 and S66). One design is based on "chopping" the scaffold of a DNA origami to short strands (fig. S65A). The other adopts standardized motifs that are each 32 nt long and have two crossovers (fig. S65B). These designs further demonstrate the versatility of DNA brick self-assembly.

Discussion

DNA bricks provide a simple, modular, and robust framework for assembling complex structures from short strands. Simplicity: A canonical brick is a standardized 32-nt single strand composed of four 8-nt binding domains; bricks interact via simple local binding rules. Modularity: With no scaffold present, an assembly of bricks has a modular architecture; each brick can be added or removed independently. Robustness: The assembly process is robust to variations in sequence composition (random sequences are used), strand synthesis (unpurified strands suffice), and stoichiometry (no tight control is required). Together, the simple and standardized motif, modular architecture, and robust performance permit straightforward automation of the design and construction process. A software tool takes as input a 3D shape specification and directs a liquid-handling robot to select and mix presynthesized brick strands to form the shape. Using a 1000-voxel canvas, 102 diverse shapes were rapidly prototyped. These shapes demonstrate a new level of geometrical sophistication, as exemplified by the intricate tunnel and cavity features.

The DNA brick framework is not restricted to the canonical 32-nt motif and can be generalized to include various other motifs (Fig. 4), enabling the construction of 3D structure with diverse lattice-packing geometries. In addition, previously demonstrated single-stranded tiles (*15*, *26*) can be viewed as a special case of bricks in which each pair of neighboring bricks form a 180° angle. For comparison, in hexagonal-, square-, and honeycomb-lattice structures, neighboring bricks form 60°, 90°, and 120° angles, respectively. These different angles are achieved by changing the domain lengths of bricks. Furthermore, neighboring bricks may be merged into a longer strand, which may facilitate nucleation or strengthen structurally weak positions. The DNA brick (and single-stranded tile) method differs from previous multistranded tiles in that each brick monomer is a floppy single strand and only folds into a bricklike shape when incorporated into the assembly. It also differs from DNA origami by not using a scaffold strand. However, DNA origami can also be related to the brick framework, in which half of the bricks are concatenated into a long scaffold (fig. S65A). The successes of constructions that use only short strands (as in bricks) and those that include a long scaffold (as in origami) together suggest a full spectrum of motif possibilities with strands of diverse lengths: Longer strands may provide better structural support, and shorter ones may provide finer modularity and features; the eclectic use of both may lead to the most rapid progression toward greater complexity.

The DNA brick structures constructed here are still far below the size limit allowed by sequence uniqueness. Making the conservative assumption (by neglecting the contribution of cooperativity) that every domain must display a different sequence, a structure using canonical 32-nt, four-domain bricks could potentially reach a size of 8 nt by 4^8 (524,288 nucleotides). In our experiments, the assembly process appeared to tolerate (sparse) identical domains (fig. S8), further expanding the potential obtainable size. Further exponential increase in size could potentially be achieved by using bricks with longer domains or by encoding algorithmic growth patterns (*8*) in

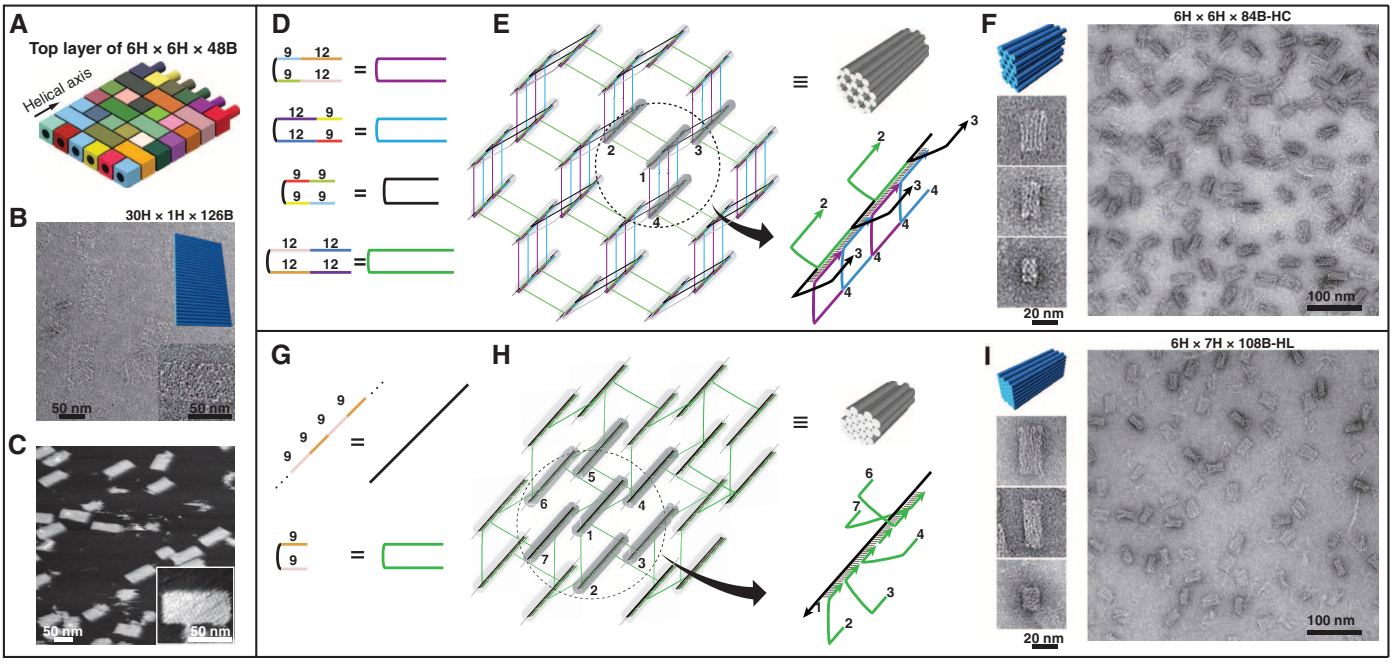

Fig. 4. Generality of DNA brick self-assembly. (**A** to **C**) The design and construction of a single-layer brick structure. (A) DNA bricks of the top layer of the 6H by 6H by 48B cuboid in Fig. 1D, with the crossovers to the layer below removed. (B) TEM images of a 30H by 1H by 126B rectangle. Top right inset shows the model of the design. Bottom right inset contains a zoomed-in image of the structure. (C) AFM images of the 30H by 1H by 126B rectangle. Inset contains a zoomed-in image of the structure. (**D** to **I**) The designs and constructions of 3D honeycomb-lattice [(D) to (F)] and hexagonal-lattice [(G) to (I)] brick structures. [(D) and (G)] The strands used for (D) honeycomb-lattice and (G) hexagonal-lattice self-assembly. The number of nucleotides in each domain is indicated in the left panel. [(E) and (H)] Strand diagrams of (E) an 84-bp honeycomb-lattice structure and (H) a 54-bp hexagonal-lattice structure. The right bottom image depicts an enlarged image of the circled helix bundle. Strand colors match those described on the right side of (D) or (G). Numbers indicate DNA helices. [(F) and (I)] TEM images of (F) a 6H by 6H by 84B-HC hexagonal-lattice structure and (I) a 6H by 7H by 108B-HL 3D hexagonal-lattice structure. 3D model and zoomed-in images of different projection views are shown to left.

the assembly. However, in practice, low yields were already observed for larger designs (up to 24,576 nucleotides attempted thus far). Solving this challenge may require improvements in structure and sequence design, enzymatic synthesis for higher-quality strands, optimized thermal or isothermal (*44*) annealing conditions, and a detailed understanding and perhaps explicit engineering of the kinetic assembly pathways (*8*, *14*, *44*) of DNA brick structures.

The DNA brick structure, with its modular architecture, sophisticated geometry control, and synthetic nature, will further expand the range of applications and challenges that nucleic acid nanotechnology has already started to address—for example, to arrange technologically relevant guest molecules into functional devices (*6*, *25*, *32*–*34*), to serve as programmable molecular probes and instruments for biological studies (*33*, *34*, *36*), to render spatial control for biosynthesis of useful products (*25*), to function as smart drug delivery particles (*37*), and to enable high-throughput nanofabrication of complex inorganic materials for electronics or photonics applications (*6*, *32*). The modularity of the brick structure may facilitate rapid prototyping of diverse functional nanodevices. Its sophisticated and refined geometrical control may enable applications that require high-precision arrangements of guest molecules. Because the brick structure is composed entirely of short synthetic strands (no biologically derived scaffold), it is conceivable to make bricks by using synthetic informational polymers other than the natural form of DNA. Such polymers may include L-DNA (*26*), DNA with chemically modified backbones or artificial bases, or chemically synthesized or in vitro (or even in vivo) transcribed RNA. This material diversity may potentially produce nanostructures with not only prescribed shapes but also designer chemical (or biochemical) properties (such as nuclease resistance or reduced immunogenicity) that would be useful for diverse applications requiring the structure to function robustly in complex environments, such as in living cells or organisms.

References and Notes

1. N. C. Seeman, *J. Theor. Biol.* **99**, 237 (1982).
2. J. H. Chen, N. C. Seeman, *Nature* **350**, 631 (1991).
3. T. J. Fu, N. C. Seeman, *Biochemistry* **32**, 3211 (1993).
4. E. Winfree, F. Liu, L. A. Wenzler, N. C. Seeman, *Nature* **394**, 539 (1998).
5. B. Yurke, A. J. Turberfield, A. P. Mills Jr., F. C. Simmel, J. L. Neumann, *Nature* **406**, 605 (2000).
6. H. Yan, S. H. Park, G. Finkelstein, J. H. Reif, T. H. LaBean, *Science* **301**, 1882 (2003).
7. W. B. Sherman, N. C. Seeman, *Nano Lett.* **4**, 1203 (2004).
8. P. W. K. Rothemund, N. Papadakis, E. Winfree, *PLoS Biol.* **2**, e424 (2004).
9. A. Chworos *et al.*, *Science* **306**, 2068 (2004).
10. S. H. Park *et al.*, *Angew. Chem. Int. Ed.* **45**, 735 (2006).
11. P. W. K. Rothemund, *Nature* **440**, 297 (2006).
12. G. Seelig, D. Soloveichik, D. Y. Zhang, E. Winfree, *Science* **314**, 1585 (2006).
13. Y. He *et al.*, *Nature* **452**, 198 (2008).
14. P. Yin, H. M. T. Choi, C. R. Calvert, N. A. Pierce, *Nature* **451**, 318 (2008).
15. P. Yin *et al.*, *Science* **321**, 824 (2008).
16. E. S. Andersen *et al.*, *Nature* **459**, 73 (2009).
17. Y. Ke *et al.*, *Nano Lett.* **9**, 2445 (2009).
18. S. M. Douglas *et al.*, *Nature* **459**, 414 (2009).
19. H. Dietz, S. M. Douglas, W. M. Shih, *Science* **325**, 725 (2009).
20. J. Zheng *et al.*, *Nature* **461**, 74 (2009).
21. T. Omabegho, R. Sha, N. C. Seeman, *Science* **324**, 67 (2009).
22. I. Severcan *et al.*, *Nat. Chem.* **2**, 772 (2010).
23. D. Han *et al.*, *Science* **332**, 342 (2011).
24. L. Qian, E. Winfree, *Science* **332**, 1196 (2011).
25. C. J. Delebecque, A. B. Lindner, P. A. Silver, F. A. Aldaye, *Science* **333**, 470 (2011).
26. B. Wei, M. Dai, P. Yin, *Nature* **485**, 623 (2012).
27. C. Lin, Y. Liu, S. Rinker, H. Yan, *ChemPhysChem* **7**, 1641 (2006).
28. N. B. Leontis, A. Lescoute, E. Westhof, *Curr. Opin. Struct. Biol.* **16**, 279 (2006).
29. W. M. Shih, C. Lin, *Curr. Opin. Struct. Biol.* **20**, 276 (2010).
30. N. C. Seeman, *Annu. Rev. Biochem.* **79**, 65 (2010).
31. D. Y. Zhang, G. Seelig, *Nat. Chem.* **3**, 103 (2011).
32. A. Kuzyk *et al.*, *Nature* **483**, 311 (2012).
33. H. M. T. Choi *et al.*, *Nat. Biotechnol.* **28**, 1208 (2010).
34. C. Lin *et al.*, *Nat. Chem.* **4**, 832 (2012).
35. M. J. Berardi, W. M. Shih, S. C. Harrison, J. J. Chou, *Nature* **476**, 109 (2011).
36. N. D. Derr *et al.*, *Science* **338**, 662 (2012).
37. S. M. Douglas, I. Bachelet, G. M. Church, *Science* **335**, 831 (2012).
38. P. W. K. Rothemund, E. S. Andersen, *Nature* **485**, 584 (2012).
39. Materials and methods, supplementary figures and texts, and DNA sequences are available as supplementary materials on *Science* Online.
40. S. M. Douglas *et al.*, *Nucleic Acids Res.* **37**, 5001 (2009).
41. Y. Ke *et al.*, *J. Am. Chem. Soc.* **131**, 15903 (2009).
42. C. E. Castro *et al.*, *Nat. Methods* **8**, 221 (2011).
43. Y. Ke, N. V. Voigt, K. V. Gothelf, W. M. Shih, *J. Am. Chem. Soc.* **134**, 1770 (2012).
44. R. Schulman, B. Yurke, E. Winfree, *Proc. Natl. Acad. Sci. U.S.A.* **109**, 6405 (2012).

Acknowledgments: The authors thank M. Dai for technical assistance; E. Winfree, B. Wei, and S. Woo for discussions; and D. Pastuszak for assistance in draft preparation. This work is supported by an Office of Naval Research (ONR) Young Investigator Program award N000141110914, an ONR grant N000141010827, an Army Research Office grant W911NF1210238, an NSF CAREER award CCF1054898, an NIH Director's New Innovator award 1DP2OD007292, and a Wyss Institute Faculty Startup Fund to P.Y., and by a Wyss Institute Faculty Grant, ONR grants N000014091118 and N000141010241, and an NIH Director's New Innovator award 1DP2OD004641 to W.M.S.. L.L.O. is supported by an NSF graduate research fellowship. Y.K. conceived the project, designed and performed the experiments, analyzed the data, and wrote the paper; L.L.O. designed and performed the experiments, analyzed the data, and wrote the paper; W.M.S. conceived the project, discussed the results, and wrote the paper; P.Y. conceived, designed, and supervised the study, interpreted the data, and wrote the paper. The DNA sequences for the nanostructures can be found in the supplementary materials. A provisional patent has been filed based on this work.

Supplementary Materials

www.sciencemag.org/cgi/content/full/338/6111/1177/DC1
Materials and Methods
Supplementary Text
Figs. S1 to S66
Tables S1 to S20

11 July 2012; accepted 16 October 2012
10.1126/science.1227268

A Reconciled Estimate of Ice-Sheet Mass Balance

Andrew Shepherd,[1]* Erik R. Ivins,[2]* Geruo A,[3] Valentina R. Barletta,[4] Mike J. Bentley,[5] Srinivas Bettadpur,[6] Kate H. Briggs,[1] David H. Bromwich,[7] René Forsberg,[4] Natalia Galin,[8] Martin Horwath,[9] Stan Jacobs,[10] Ian Joughin,[11] Matt A. King,[12,27] Jan T. M. Lenaerts,[13] Jilu Li,[14] Stefan R. M. Ligtenberg,[13] Adrian Luckman,[15] Scott B. Luthcke,[16] Malcolm McMillan,[1] Rakia Meister,[8] Glenn Milne,[17] Jeremie Mouginot,[18] Alan Muir,[8] Julien P. Nicolas,[7] John Paden,[14] Antony J. Payne,[19] Hamish Pritchard,[20] Eric Rignot,[18,2] Helmut Rott,[21] Louise Sandberg Sørensen,[4] Ted A. Scambos,[22] Bernd Scheuchl,[18] Ernst J. O. Schrama,[23] Ben Smith,[11] Aud V. Sundal,[1] Jan H. van Angelen,[13] Willem J. van de Berg,[13] Michiel R. van den Broeke,[13] David G. Vaughan,[20] Isabella Velicogna,[18,2] John Wahr,[3] Pippa L. Whitehouse,[5] Duncan J. Wingham,[8] Donghui Yi,[24] Duncan Young,[25] H. Jay Zwally[26]

We combined an ensemble of satellite altimetry, interferometry, and gravimetry data sets using common geographical regions, time intervals, and models of surface mass balance and glacial isostatic adjustment to estimate the mass balance of Earth's polar ice sheets. We find that there is good agreement between different satellite methods—especially in Greenland and West Antarctica—and that combining satellite data sets leads to greater certainty. Between 1992 and 2011, the ice sheets of Greenland, East Antarctica, West Antarctica, and the Antarctic Peninsula changed in mass by −142 ± 49, +14 ± 43, −65 ± 26, and −20 ± 14 gigatonnes year^{-1}, respectively. Since 1992, the polar ice sheets have contributed, on average, 0.59 ± 0.20 millimeter year^{-1} to the rate of global sea-level rise.

Fluctuations in the mass of the polar ice sheets are of considerable societal importance, because they affect global sea levels (*1*, *2*) and oceanic conditions. They occur as a consequence of their internal dynamics and changes in atmospheric and oceanic conditions (*3*–*5*). Analysis of the geological record suggests that past climatic changes have precipitated